Nanofabrication of 50 nm zone plates through e-beam lithography with local proximity effect correction for x-ray imaging[*]

Jingyuan Zhu(朱静远)[1], Sichao Zhang(张思超)[1], Shanshan Xie(谢珊珊)[1], Chen Xu(徐晨)[1],
Lijuan Zhang(张丽娟)[2], Xulei Tao(陶旭磊)[2], Yuqi Ren(任玉琦)[2], Yudan Wang(王玉丹)[2],
Biao Deng(邓彪)[2], Renzhong Tai(邰仁忠)[2], and Yifang Chen(陈宜方)[1,†]

[1] *Nanolithography and Application Research Group, State Key Laboratory of Asic and System,*
School of Information Science and Engineering, Fudan University, Shanghai 200433, China

[2] *Shanghai Synchrotron Radiation Facility, Shanghai Institute of Applied Physics, Chinese Academy of Sciences, Shanghai 201204, China*

High resolution Fresnel zone plates for nanoscale three-dimensional imaging of materials by both soft and hard x-rays are increasingly needed by the broad applications in nanoscience and nanotechnology. When the outmost zone-width is shrinking down to 50 nm or even below, patterning the zone plates with high aspect ratio by electron beam lithography still remains a challenge because of the proximity effect. The uneven charge distribution in the exposed resist is still frequently observed even after standard proximity effect correction (PEC), because of the large variety in the line width. This work develops a new strategy, nicknamed as local proximity effect correction (LPEC), efficiently modifying the deposited energy over the whole zone plate on the top of proximity effect correction. By this way, 50 nm zone plates with the aspect ratio from 4 : 1 up to 15 : 1 and the duty cycle close to 0.5 have been fabricated. Their imaging capability in soft (1.3 keV) and hard (9 keV) x-ray, respectively, has been demonstrated in Shanghai Synchrotron Radiation Facility (SSRF) with the resolution of 50 nm. The local proximity effect correction developed in this work should also be generally significant for the generation of zone plates with high resolutions beyond 50 nm.

Keywords: Fresnel zone plates, electron beam lithography, local proximity effect correction, x-ray imaging, 50 nm resolution

PACS: 75.75.Cd, 07.85.–m, 41.50.+h   **DOI:** 10.1088/1674-1056/ab7800

1. Introduction

Nowadays, material physics, especially magnetic nanocomposites, is developing rapidly around the world.[1–7] As the research scale gradually advances to nanosize,[8–13] there are growing needs to develop microscopes for observing the inside structure of materials at molecular level.[14] High resolution x-ray microscopy, such as full-field transmission x-ray microscope (TXM), is one of the most powerful techniques for imaging objects with unique advantages of noninvasive, non-destructive, three-dimensional, real time, and high resolution over other microscopes. Because of this, extensive applications of TXMs can be found in material science, life science, medical diagnosis, environmental monitoring and protection, integrated circuits (ICs) manufacturing technology, etc.[15] The key optics in a TXM is the Fresnel zone plates (FZPs) in noble metals, used as a focusing and imaging lens based on the first order diffraction of the transmitted x-ray. So far, there have been many methods for manufacturing the zone plates, including sputtering/dicing,[16–19] atomic layer deposition (ALD) for narrow zones,[20–22] reactive ion etch combined with Au electroplating[23–27] and electron beam lithography (EBL) ended by electroplating.[28–31] However, the mainstream of the fabrication technique is still EBL com-

bined with metal electroplating because it has proved to be the most stable and reliable process. Although this technique has advanced to 12 nm resolution,[32] which is proportional to the outmost zone-width by a factor of 1.22, both the zone shaping and the sizing in EBL, which determine the diffraction efficiency, have still been hardly addressed in detail. As already established, the maximum diffraction efficiency of a 600-nm-tall Au FZP, for example, is 9.8% for 9 keV photon energy when the duty cycle, i.e., the metal zone-width over the metal plus air width, is 0.5.[33] However, the efficiency will drop to half of the maximum value if the duty cycle becomes either 0.25 or 0.75. Not only this, the zone shape such as the side-wall verticality greatly influences the imaging efficiency. Therefore, it is necessary to study how to control the zone profile by EBL condition for forming the metallic zones with the desired duty cycle and zone shape of the resultant FZPs.

This paper concentrates on the study of the resist profile control by modifying the injected charge-distribution in resist in the nanofabrication of 50 nm FZPs. It was found that the existing method of proximity effect correction (PEC) by BEAMER/TRACER/LAB software delivered by GenISys Ltd was difficult to achieve the uniform charge distribution over the whole zone plate because of the large variation in the line-

[†]Corresponding author. E-mail: yifangchen@fudan.edu.cn

width. Especially in the region of the outmost zones, the local modification of PEC by a manual method, developed in this work, was necessary to further control the zone shape and size. By utilizing the locally modified dose distribution, electron beam lithography was carried out and 50 nm zone plates with aspect ratio of 15:1 for hard x-ray and 4:1 for soft x-ray, respectively, were successfully fabricated. X-ray imagings at 1.3 keV and 9 keV, respectively, were demonstrated with 50 nm resolution in Shanghai Synchrotron Radiation Facility (SSRF).

2. Local proximity effect correction of the charge exposure

In this work, the zone plate to be fabricated has the outmost zone-width of 50 nm and the radius of 50 μm on a 100-nm thick Si_3N_4 membrane. The proximity effect should be mainly caused by the forward scattering electrons. Since the lack of contrast curves as well as the dissolution rates from the resist coated on a free-standing membrane, the proximity effect correction for figuring out the optimized exposure dose was carried out in a 4-μm thick PMMA (molecular weight: 350k) on Si substrate, where the extra exposure by backscattered electrons from the substrate could be neglected. The local proximity effect correction was carried out by the following procedure. First, the point-spread function (PSF) of the injected electrons at 100 keV was calculated by the TRACER software with Monte Carlo method (10^6 electrons were used in the simulation). Figure 1 presents the PSFs in PMMA at the depth of 625 nm from the surface in the layer-stacks of PMMA(4 μm)/Si(500 μm) and PMMA(650 nm)/Au(15 nm)/Cr(5 nm)/Si_3N_4(100 nm), respectively. It can be clearly seen that these two PSF curves coincide with each other extremely well in the radius < 1 μm, indicating that the 4 μm thick PMMA coated on Si can precisely represent the 650-nm thick PMMA coated on the Au/Cr/Si_3N_4 membrane system as an outstanding simulator in the radius below 1 μm. Beyond 1 μm, although there is a significant difference between these two point-spread functions, the backscattered charge is merely 10^{-6} of the forward scattered one (radius < 1 μm). Therefore, the extra exposure by backscattered electrons in the 4-μm PMMA/Si can be neglected as in the resist on the Si_3N_4 membrane.[34]

Based on the simulated PSF curve, the deposited energy distribution in the PMMA coated on the SiN_x membrane was first calculated by convoluting the PSF with the designed zone plate pattern without PEC. Figure 2(a) presents the spatial distribution of the deposited charge at the depth of 625 nm in the PMMA for the three different regions of the zone plate as marked in Fig. 2. Apparently, exposed with such a distribution, large variations in zone-depths and zone-widths were observed between different regions after development. On one

hand, the zones in the central region were deeper and wider than the designed ones, induced by the extra charge from their neighboring zones. On the other hand, those in the outmost region suffered from under exposure condition, arising from the lack of contribution by secondary electrons from the surrounding zones. PEC using BEAMER was then carried out and the corrected charge distribution is shown in Fig. 2(b). Unfortunately, the injected charge difference of 120 μC/cm^2 between the central part and the outmost zone can still be seen. This is because the TRACER is not able to deal with every region locally. Therefore, a manual method to locally correct the exposure charge was carried out.
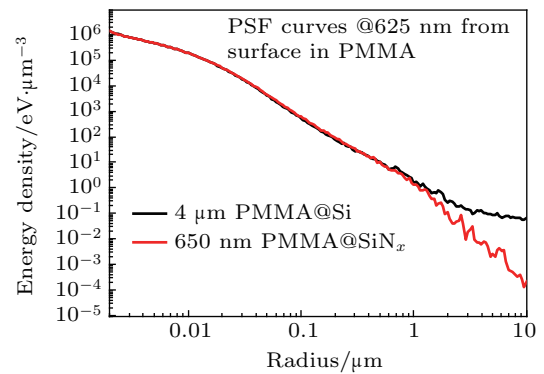

Fig. 1. PSF curves at 625 nm from surface in PMMA, the red curve is from 650 nm PMMA on SiN_x membrane and the black is from 4 μm PMMA on Si.
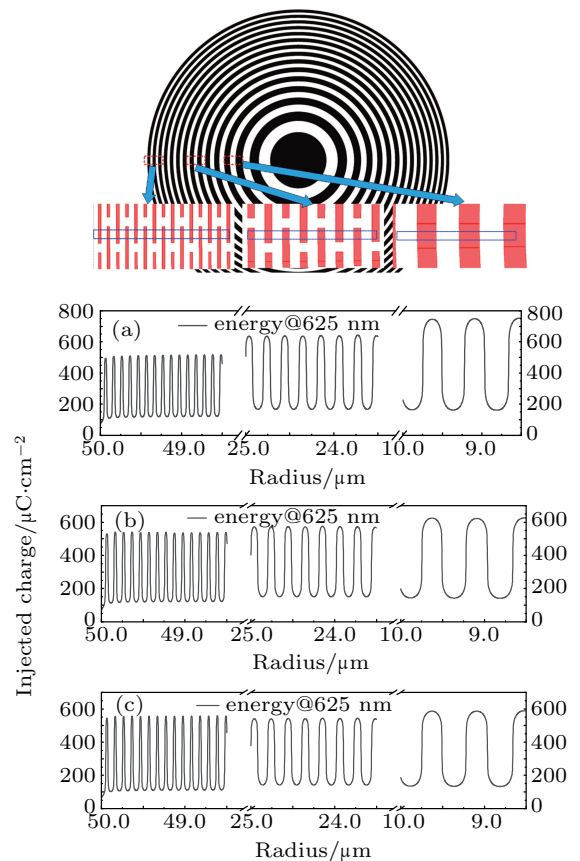

Fig. 2. Numerical simulations of charge distributions at the depth of 625 nm from the surface of 4-μm PMMA with three different correction methods: (a) without PEC, (b) with a computer generated PEC, and (c) with local PEC.

The local proximity effect correction (LPEC) in manual way was undertaken based on the computer generated PEC result shown in Fig. 2(b). The zone pattern was divided into 3 areas: in the 0–19 μm radius zone (ring width range: 127–710 nm), the exposure doses were manually reduced by 50% of the computer generated PEC value; in the 19–34 μm radius zone (ring width range: 71.4–127 nm), the exposure doses were unchanged; in the 34–50 μm radius zone (ring width range: 50–71.4 nm), the exposure doses were manually increased by 20%. Meanwhile, to avoid the zone widening, sizing of −20 nm was carried out in the pattern design. The charge distribution at the depth of 625 nm in PMMA with such a modification was worked out, as presented in Fig. 2(c). The most even charge distribution was achieved by LPEC among the three methods. Furthermore, the contrast curves of the PMMA normalized to 4-μm-thickness and the corresponding dissolution rates, obtained by our earlier work,[34] were applied to simulate the resultant resist profiles based on the calculated charge distributions in Fig. 2. In this simulation, the dynamic development process was simulated by the LAB simulator.

Figure 3 presents the simulated resist profiles for the three distributions of deposited energy as discussed above. In the three simulations, the same exposure base dose of 1170 μC/cm^2 was used. The duty cycles of the outmost zones were compared and summarized in Table 1 for the three charge distributions. Since the trench sidewalls were not vertical, the maximum width of the trench was taken in the calculation of duty cycles. From Fig. 3 and Table 1, it can be concluded as follows. First, among the three methods, LPEC gives rise to the most vertical sidewall of the zones. Second, the duty cycles by LPEC are closest to 0.5 in the three methods. In the dose distribution without PEC, the central part was totally over exposed, resulting in the collapse of the zones. Finally, the height difference in the zone plate by LPEC was the smallest among the three methods. Therefore, the LPEC method developed in this work was applied in the nanofabrication of 50 nm zone plates with high aspect ratio.
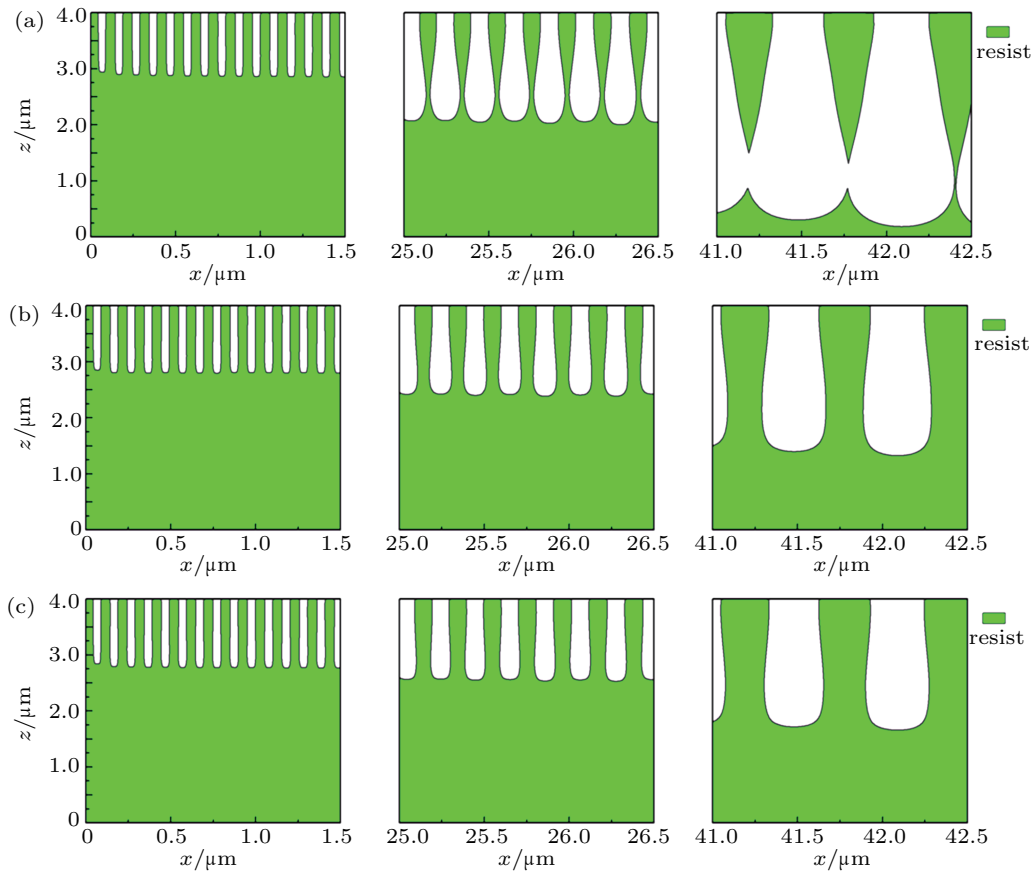

Fig. 3. The simulation results of development for the resist profiles by three different correction methods: (a) no PEC, (b) PEC, and (c) LPEC. Apparently, the LPEC in dose resulted in the best profile comparing to the other two.

Table 1. The comparison of the duty cycles in the zone plate by three different correction methods.

Zone region	No PEC	Computer PEC	Local PEC
0–1.5 μm	45.10%	47.05%	48.51%
25–26.5 μm	90%	66.33%	58.82%
41–42.5 μm	100%	65.63%	54.02%

3. Fabrication process and results

Nanofabrication results of 50 nm zone plates using the three different correction methods in EBL, i.e., without PEC, with computer generated PEC, and with manual LPEC, respectively, were also compared. The samples were prepared

on the in-house made 100 nm Si_3N_4 membranes. First of all, a seed layer of 5 nm Cr/15 nm Au for gold electroplating was coated by thermal evaporation in vacuum. Secondly, 650-nm-thick PMMA (MW: 350k) was spin coated and then baked in an oven for 1 h at 180 ℃. E-beam exposure for the zone plates was carried out by a state-of-the-art e-beam writer (JEOL 6300FS) with a Gaussian beam at 100 keV. The beam current used was 500 pA to ensure the beam-spot diameter of 7–10 nm.

After the E-beam exposure, the samples were developed in methyl isobutyl ketone (MIBK)/iso-propyl alcohol (IPA) (1 : 3) for 60 s at 23 ℃, and finally rinsed in IPA. And before the electroplating of Au, the samples were washed in O_2 plasma by an etcher (RIE, Samco, 10NR) to remove the resist left on the trench bottom. Au electroplating was carried out in a $K_3Au(SO_3)_2$ electrolyte (10 g/L concentration, PH 9.5, 50 ℃, supplied by Metalor Ltd), driven by a constant current source delivered by Keithley Ltd. The plating rate of Au was strictly maintained around 100 nm/min at the temperature of 50 ℃. The electroplating was immediately terminated when the zone trenches in PMMA were filled by the plating gold to the pre-set height. Finally, a liftoff process was done by soaking the plated zone plates in acetone for about 10 min to remove the unwanted resist area.

Figure 4 presents the comparisons of the zone plates respectively fabricated by the three different PEC methods. The FZP without PEC gives rise to the incomplete plate, as shown in Figs. 4(a) and 4(b) due to the under exposure condition in the outmost zones, as numerically predicted in Fig. 3(a). Although the one with computer generated PEC, as presented in Fig. 3(b), does show improvement in the outmost zones, some missing zones are still observed because of the charge shortage in that area (Figs. 4(c) and 4(d)). Increasing the base dose could make the outmost zones properly developed, but the

zone widths in the central part would definitely be enlarged, causing the reduction of the duty cycle, which may lead to the reduction of the diffraction efficiency. This is ascribed simply to the large difference of the deposited charge between the center and the outmost zones, as simulated in Fig. 3(b). The local PEC developed in this work makes the best balance of charge distribution in the whole zone plate among the three methods, giving rise to the most complete zone plate as shown in Figs. 4(e) and 4(f). High quality Fresnel zone plates were successfully fabricated for both soft and hard x-ray optics.
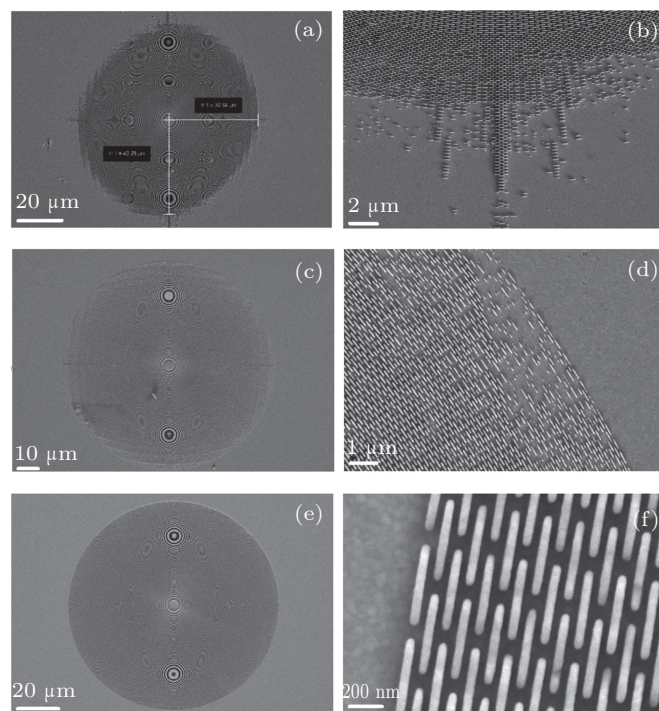

Fig. 4. Comparisons of the resultant zone plates after electroplating of Au and lift off process, exposed by three different charge distributions, respectively. (a), (b) The zone plates without any proximity correction. (c), (d) The plates with computer generated correction. (e), (f) The plates with local PEC on the top of PEC in (c).
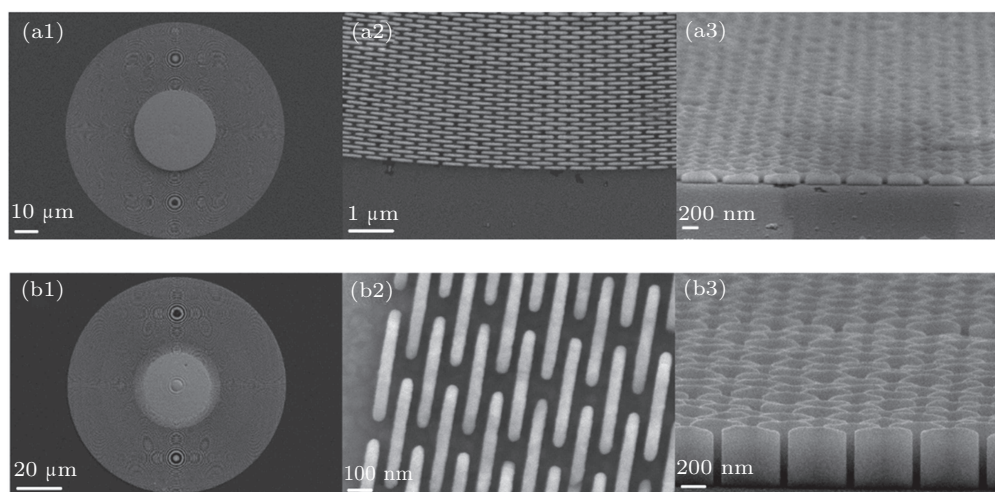

Fig. 5. SEM micrographs of the fabricated zone plates by EBL with local PEC and Au electroplating. (a) The FZPs with the aspect ratio of 4 : 1 for soft x-ray. The central part is an integrated 2-μm-thick beam stop. (b) The FZPs with the aspect ratio of 15 : 1. The photos in (a3) and (b3) were taken at the SE2 tilt angle of 70°.

Based on the optimized base dose range of 1000–1200 $\mu C/cm^2$ with LPEC, 50 nm Fresnel zone plates respectivley for soft x-ray at 1.3 keV and hard x-ray at 9 keV were fabricated. Figure 5 presents the micrographs of the fabricated zone plates, taken by the scanning electron microscope (SEM), Sigma HD, delivered by ZEISS Ltd. Figure 5(a) shows the zone plates in gold with the outmost zone-width of 50 nm and the zone height of 200 nm, standing on the 100 nm-thick Si_3N_4 membranes for the soft x-ray at 1.3 keV. Figure 5(b) shows the zone plate with the same layout as that in Fig. 5(a) but the zone height of 750 nm for the hard x-ray at 9 keV. The aspect ratio (height/zone-width) as high as 15 : 1 was achieved by utilizing the LPEC method in this work.

For soft x-ray imaging, a beam stop of a gold disc with the diameter of 40 μm and the thickness of 2 μm in the center of the zone plate was needed. The integration of such a gold disc to the fabricated zone plate was carried out by the second EBL with registration technique, followed by Au plating. A high quality beam stop can been seen in the center of the 50 nm zone plate in Fig. 5(a).

4. Sub 60 nm x-ray imagining by the fabricated FZPs

Demonstrations of x-ray imaging by the fabricated 50 nm FZPs were carried out in SSRF. For soft x-ray imaging at the photon energy of 1.3 keV, Siemens stars in gold with 50–60 nm resolution and 900 nm height, as the object, were first fabricated, which will be reported in other occasion. The fabricated zone plate in Au as the lens has the thickness of 200 nm, the outmost zone-width of 50 nm, the focusing length of 5241.9 μm, the radius of 50 μm, and the number of zones of 500. Required by the particular optical system in SSRF,

the zone plate has a built-in beam-stop with the diameter of 40 μm and the thickness of 2 μm. The whole FZP was free standing on a 100-nm-thickness Si_3N_4 membrane. Figure 6 shows the soft x-ray imaging of the Siemens star by the FZP at 1.3 keV. Figures 6(a) and 6(b) are the SEM photos of the Siemens star as the object. Figures 6(c) and 6(d) are the x-ray photos taken by the scanning STXM system (BL08U1-A beamline). The resolution of the STXM system is equal to the step of the sample stepper motor, which is 15 nm. According to the x-ray micrographs in Figs. 6(c) and 6(d), the lines about 60 nm wide in the test patterns can be identified in the images. The transmittance of the Si_3N_4 membrane for 1.3 keV soft x-ray is 92.6%.

Hard x-ray imaging at 9 keV was also demonstrated by the TXM system (BL13W1 beamline) using the fabricated FZP in Au with the thickness of 600 nm and the focusing length of 36.290 mm. The resolution capability of the TXM system is 25 nm. The zone plate was free standing on a 100 nm thick Si_3N_4 membrane through which the transmittance of the x-ray at 9 keV is 99.93%. Figure 7 shows the hard x-ray imaging photos of the Siemens star, delivered by NTT Advanced Technology Corporation.

Figures 7(a) and 7(b) show the SEM photos of the Siemens star used as the object, and figures 7(c) and 7(d) present the images of the Siemens star shown in Figs. 7(a) and 7(b). The 50–60 nm-wide lines in the test patterns, can be identified in the x-ray micrograph images, as shown in Figs. 7(c) and 7(d). The clear contrast shown in both x-ray images proves the good quality of the fabricated Fresnel zone plates. It is believed that more exiting advances are expected to come based on the rapid development of nanofabrication technique in our laboratory.
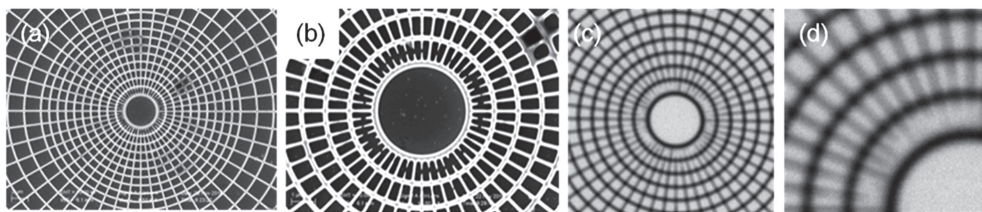

Fig. 6. Demonstration of the soft x-ray imaging by the fabricated 50 nm zone plates in this work. (a) and (b) The SEM photos for the Siemens star with 50–60 nm wide lines as the thinnest feature in the center. The height of the star is 900 nm. The star was used in this imaging as the object. (c) and (d) Soft x-ray imaging photos of the object in (a) and (b), taken at 1.3 keV by STXM system.
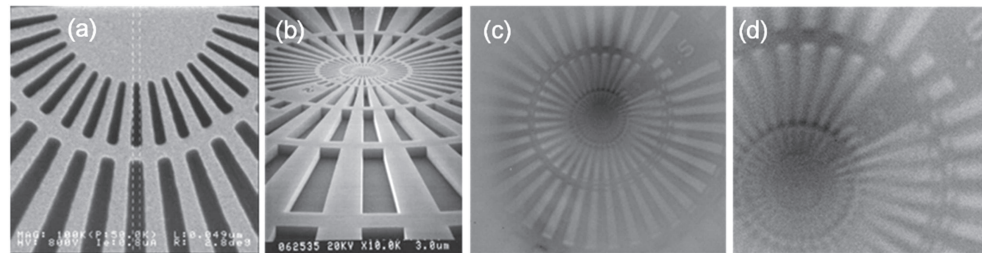

Fig. 7. Demonstration of the hard x-ray imaging by the fabricated 50 nm zone plates in this work. (a) and (b) The SEM photos for the in-house fabricated Siemens star with 50–60 nm wide lines as the thinnest feature in the center. The height of the star is 500 nm. The star was used in this imaging as the object. (c) and (d) Hard x-ray imaging photos of the object in (a) and (b), taken at 9 keV by TXM system.

5. Conclusion

This paper reports a new method to locally adjust the e-beam exposure dose on the basis of proximity effect correction in electron beam lithography for fabricating 50 nm zone plates applied in x-ray optics. Both numerical simulation and processing study have proved that the LPEC developed in this work is able to generate more even e-beam exposure in the whole zone plate than the conventional PEC. 50 nm zone plates in Au with the aspect ratio from 4 : 1 (for soft x-ray) up to 15 : 1 (for hard x-ray) were successfully fabricated. Optical imagings in soft and hard x-ray of the fabricated zone plates were characterized. The achieved imaging results at 1.3 keV and 9 keV demonstrate sub-60 nm resolution of the FZPs. Systemic study of the diffraction efficiency of the plates is still under way in SSRF.

References

[1] Zhang Y H and Shi J R 2015 *Chin. Phys. Lett.* **32** 37101
[2] He X M, Zhong W and Du Y W 2018 *Acta Phys. Sin.* **67** 227501 (in Chinese)
[3] Huang Y H, Jiang D L, Zhang H, Chen Z M and Huang Z R 2017 *Acta Phys. Sin.* **66** 017501 (in Chinese)
[4] Li J, Zhang H W, Li Y X, Li Q and Qin J F 2012 *Acta Phys. Sin.* **61** 227501 (in Chinese)
[5] Mehran E, Shayesteh F S and Sheykhan M 2016 *Chin. Phys. B* **25** 107504
[6] Xie Q, Wang W P, Xie Z, Zhan P, Li Z C and Zhang Z J 2015 *Chin. Phys. B* **24** 057503
[7] Cai P, Chen H M and Xie J 2014 *Chin. Phys. B* **23** 117504
[8] Pan D, Wang S L, Wang H L, Yu X Z, Wang X L and Zhao J H 2014 *Chin. Phys. Lett.* **31** 078103
[9] Meng L R, Chen W M, Chen C P, Zhou H P and Peng Q 2010 *Chin. Phys. Lett.* **27** 128101
[10] He L Z, Qin L R, Zhao J W, Yin Y Y, Yang Y and Li G Q 2016 *Chin. Phys. B* **25** 086101
[11] Liu X L, Yang Y, Wu J P, Zhang Y F, Fan H M and Ding J 2015 *Chin. Phys. B* **24** 127505
[12] Su Y K, Yan Z L, Wu X M, Liu H, Ren X and Yang H T 2015 *Chin. Phys. B* **24** 107505
[13] Zuo W L, Zhao X, Xiong J F, Shan R X, Zhang M, Hu F X, Sun J R and Shen B G 2015 *Chin. Phys. B* **24** 077103
[14] Kang H C, Maser J, Stephenson G B, Liu C, Conley R, Macrander A T and Vogt S 2006 *Phys. Rev. Lett.* **96** 127401
[15] Sakdinawat A and Attwood D 2010 *Nat. Photon.* **4** 840
[16] Doring F, Robisch A L, Eberl C, Osterhoff M, Ruhlandt A, Liese T, Schlenkrich F, Hoffmann S, Bartels M, Salditt T and Krebs H U 2013 *Opt. Express* **21** 19311
[17] Mayer M, Keskinbora K, Grevent C, Szeghalmi A, Knez M, Weigand M, Snigirev A, Snigireva I and Schutz G 2014 *J. Synchrotron Radiat.* **21** 640
[18] Kamijo N, Suzuki Y, Takano H, Tamura S, Yasumoto M, Takeuchi A and Awaji M 2003 *Rev. Sci. Instrum.* **74** 5101
[19] Shu J H, Chen Z Y, Pu J X and Liu Y X 2011 *Chin. Phys. B* **20** 114202
[20] Moldovan N, Divan R, Zeng H J, Ocola L E, De Andrade V and Wojcik M 2018 *J. Vac. Sci. Technol. A* **36** 01A124
[21] Vila-Comamala J, Jefimovs K, Raabe J, Pilvi T, Fink R H, Senoner M, Maassdorf A, Ritala M and David C 2009 *Ultramicroscopy* **109** 1360
[22] Vila-Comamala J, Gorelick S, Farm E, Kewish C M, Diaz A, Barrett R, Guzenko V A, Ritala M and David C 2011 *Opt. Express* **19** 175
[23] Reinspach J, Lindblom M, Bertilson M, Hofsten O v, Hertz H M and Holmberg A 2011 *J. Vac. Sci. Technol. B* **29** 011012
[24] Feng Y, Feser M, Lyon A, Rishton S, Zeng X H, Chen S, Sassolini S and Yun W B 2007 *J. Vac. Sci. Technol. B* **25** 2004
[25] Peuker M 2001 *Appl. Phys. Lett.* **78** 2208
[26] David C, Medenwaldt R, Thieme J, Guttmann P, Rudolph D and Schmahl G 1992 *J. Opt.* **23** 255
[27] Parfeniukas K, Rahomaki J, Giakoumidis S, Seiboth F, Wittwer F, Schroer C G and Vogt U 2016 *Microelectron. Eng.* **152** 6
[28] Gorelick S, Vila-Comamala J, Guzenko V A, Barrett R, Salome M and David C 2011 *J. Synchrotron Radiat.* **18** 442
[29] Chen Y T, Lo T N, Chiu CmW, Wang JnY, Wang C L, Liu C J, Wu S R, Jeng S T, Yang C C, Shiue J, Chen C H, Hwu Y, Yin G C, Lin H M, Je J H and Margaritondo G 2008 *J. Synchrotron Radiat.* **15** 170
[30] Gorelick S, Vila-Comamala J, Guzenko V A and David C 2011 *Microelectron. Eng.* **88** 2259
[31] Guzenko V A, Romijn J, Vila-Comamala J, Gorelick S and David C 2011 *Aip. Conf. Proc.* **1365** 92
[32] Chao W, Fischer P, Tyliszczak T, Rekawa S, Anderson E and Naulleau P 2012 *Opt. Express* **20** 9777
[33] Kirz J 1974 *J. Opt. Soc. Am.* **64** 301
[34] Liu J P, Shao J H, Zhang S C, Ma Y Q, Taksatorn N, Mao C W, Chen Y F, Deng B and Xiao T Q 2015 *Appl. Opt.* **54** 9630